Supporting Information

Strong Magnetic Exchange Coupling in a Radical-Bridged Trinuclear Nickel Complex

Luming Yang, Julius J. Oppenheim, Mircea Dincă*

Department of Chemistry, Massachusetts Institute of Technology, 77 Massachusetts Avenue, Cambridge, Massachusetts 02139, United States.

*mdinca@mit.edu

Table of Contents

Experimental methods

Tp^{Ph}NiCl and HATP·6HCl were synthesized based on previous reports.[1,2] Tetrabutylammonium hydroxide (1M solution in MeOH, AcroSeal), tetrahydrofuran (99.9%, Extra Dry, anhydrous), and toluene (99.8%, Extra Dry, anhydrous) were purchased from ACROS Organics. Tetrabutylammonium hexafluorophosphate (≥99.0%) was purchased from Sigma-Aldrich. Dichloromethane (ACS, ≥99.5%) and hexanes (ACS, ≥98.5%) were purchased from Macron Fine Chemicals. n-hexane (95+%) was purchased from Fisher Scientific. Ethanol (anhydrous, 200 Proof) was purchased from KOPTEC. Dry and deaerated solvents were stored over 4 Å molecular sieves in a nitrogen glovebox.

Synthesis of **1**: Inside a nitrogen-filled glovebox, 0.44 mL 1M methanol solution of tetrabutylammonium hydroxide (0.44 mmol) is added dropwise to a solution of 18.4 mg HATP·6HCl (0.033 mmol) dissolved in 5 mL methanol upon stirring. The mixture is then added dropwise to a solution mixture of 77 mg (Tp^{Ph}Ni)Cl (0.1 mmol) dissolved in 10 mL dichloromethane in air, exerting a color change from pink to yellow-green and blue-black. The mixture is stirred in air for 14 hr, after which the solvent is evaporated. The resulting solid is washed with methanol, hexane, and dried under vacuum, giving purple-black solid with 54% yield. Prism-like purple crystals suitable for single-crystal X-ray diffraction is obtained by recrystallization from dichloromethane-n-hexane. Elemental analysis was performed on the grinded sample underwent magnetic measurements, calculated for $C_{153}H_{114}B_3N_{24}Ni_3$·0.5($CH_2Cl_2$)·0.5($C_6H_{14}$): C, 72.78%; H, 4.76%; N, 13.02%. Found: C, 72.85%; H, 4.76%; N, 13.06%.

Elemental analyses were performed by Robertson Microlit Laboratories, Ledgewood, NJ, USA.

Single crystal XRD measurements were performed with Bruker D8 diffractometer coupled to a Bruker APEX-II CCD detector with Mo Kα radiation (λ = 0.71073 Å), performing ϕ- and ω-scans. The structure was solved by direct methods SHELXS and refined against F^2 on all data by full-matrix least squares with SHELXL-13.[3] All non-hydrogen atoms were refined anisotropically. All hydrogen atoms were included in the model at geometrically calculated positions and refined using a riding model. Details for the data quality and summary of the residual values of the refinements can be found in Table S3.

ESI/MS measurements were performed with high-resolution Agilent 6545 mass spectrometer with Jet Stream ESI source coupled to an Agilent Infinity 1260 LC system.

Continuous shape measurements were calculated with the Shape program.[4]

Electrochemical measurements were performed in 0.15 M tetrabutylammonium hexafluorophosphate solution in tetrahydrofuran containing 8 μM compound **1**, with glassy carbon working electrode, Pt mesh counter electrode, and Ag/AgCl wire pseudo-reference electrode. Working and counter electrodes were cleaned by soaking in dimethyl sulfoxide and dichloromethane followed by rinsing with acetone and drying under a stream of air. Ag/AgCl wire was made by dipping polished

Ag wire in bleach for 30 min followed by rinsing with water and acetone. Glassy carbon working electrode is further polished with 1, 0.3, and 0.05 μm diameter alumina powder from BASI. All electrochemical experiments were performed under nitrogen atmosphere with a CHI600D potentiostat, with internal resistance compensated for every experiment. Cyclic voltammograms were collected at scan rate of 100 mV·s^{-1}.

Magnetometry measurements were performed on ground single crystals with Quantum Design Dynacool D-209 Physical Property Measurement System (PPMS). Magnetization measurements were performed at 1.8 K in field range of ±90 kOe. Susceptibility measurements were performed under 1.0 kOe and 10 kOe external field in temperature range of 1.8-300 K. Experimental data were corrected for diamagnetic contribution based on blank sample holder measurements and Pascal's constants, and was fitted to the Hamiltonians described in the main text using the software *PHI*.[5]

EPR measurements were performed on frozen glasses of toluene solution of **1** with a Bruker EMX spectrometer equipped with an ER4119HS high sensitivity X-band resonator at 9.37 GHz. Temperature control was achieved by a Bruker/ColdEdge 4K waveguide cryogen-free cryostat. EPR simulations were performed with the EasySpin package (6.0.0-dev.33) in Matlab (R2020a).[6]

Computational analyses were performed using ORCA 4.2.0 quantum chemistry package.[7,8] The geometry for the clusters was extracted from the crystal structure without further optimization. Spin and charge density, as well as broken-symmetry analyses of **1** were calculated at the BP86/def2-TZVP level for Ni and def2-SVP level for other atoms using the resolution of identity (RI) approximation with S = 1/2.[9,10]
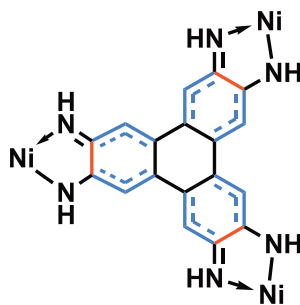
Reaction scheme for the synthesis of 1
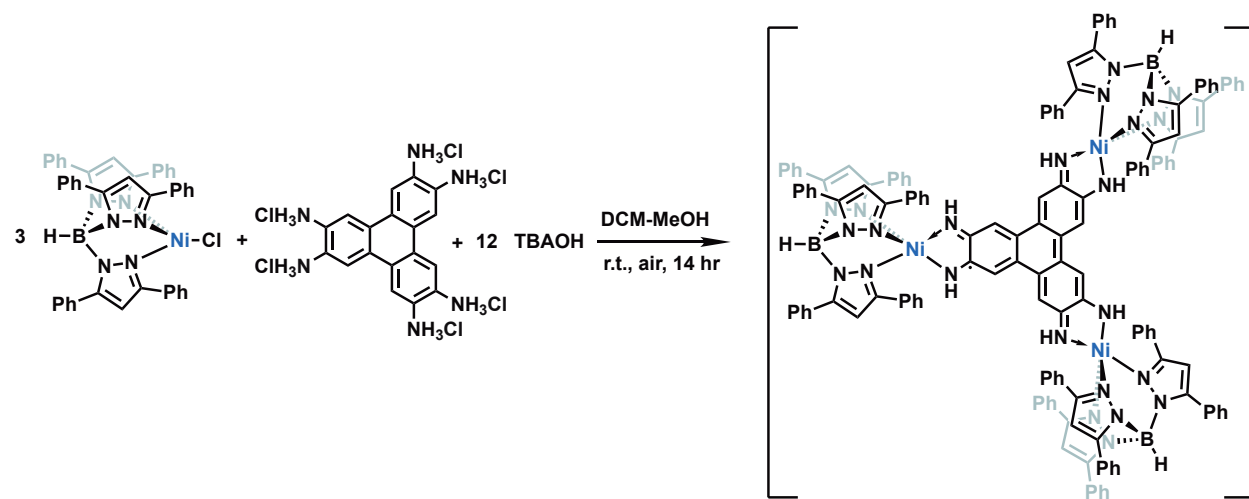
Scheme S1. Synthetic scheme of **1**, with only one possible Lewis resonance structure depicted.

Mass spectrum of 1
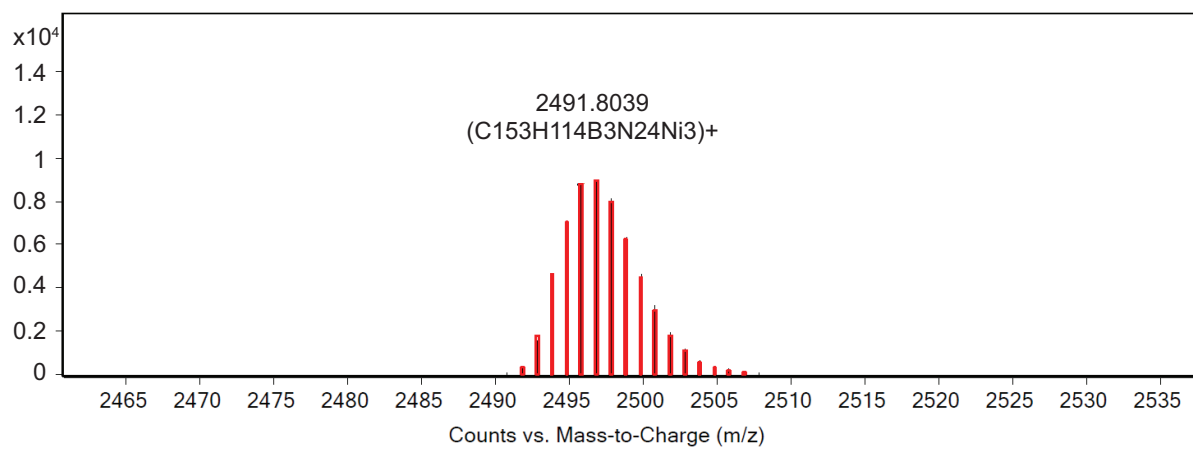
Figure S1. ESI-MS spectrum of **1** in positive-ion mode. The black lines represent experimental signals and the red bars represent predicted isotopic patterns.

Illustration of "bisallyl" motifs in 1

Scheme S2. Bond length inhomogeneities in **1**. Blue dashed bonds and red solid bonds represent the "bisallyl" motifs (vide infra) and the interspacing bonds, respectively. This scheme also shows the three Ni(BQDI) subunits of **1**.

Illustrations of geometric distortions of the HITP plane in 1
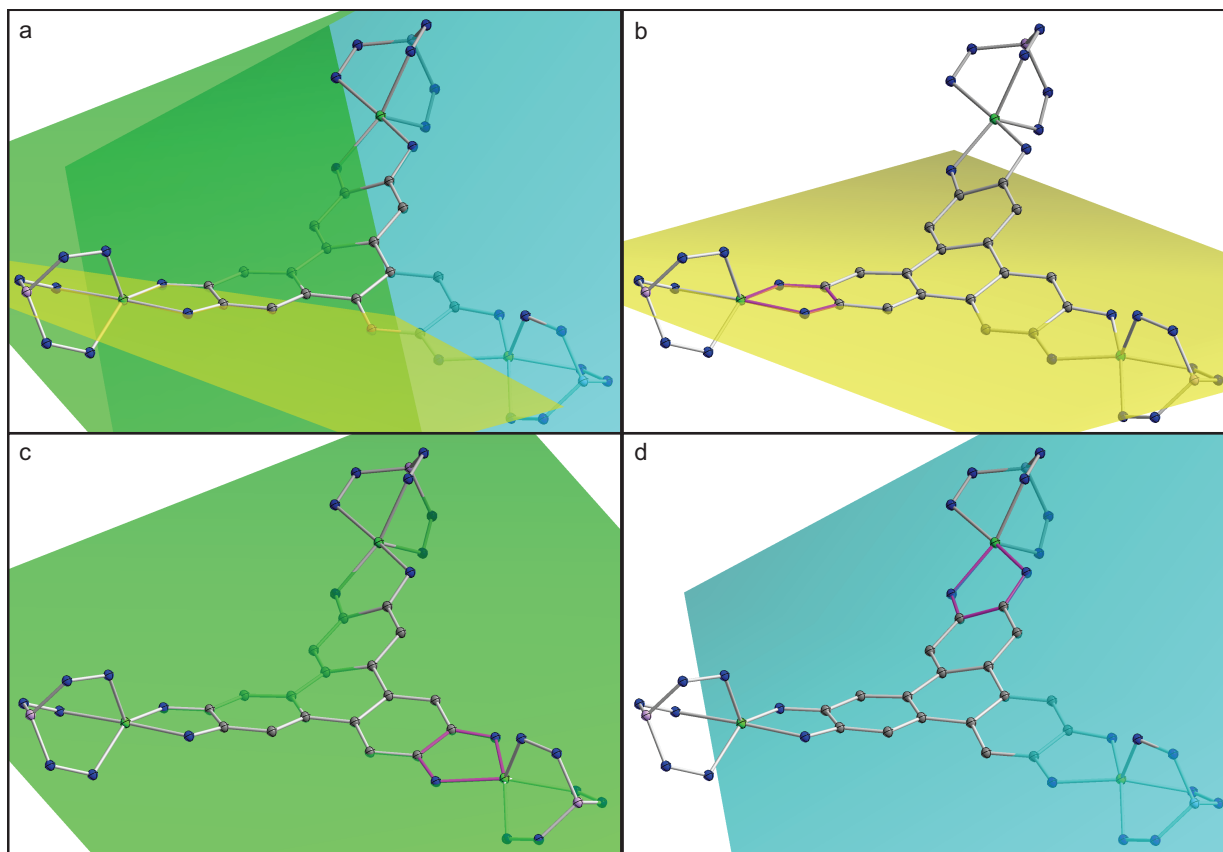
Figure S2. Geometric distortion from planarity of the HITP moiety based on single-crystal structure of **1**, with yellow, green, and turquois planes representing planes shared by the three Ni-N-C-C-N metallocycles. (a) Spatial relationship of the three planes. (b-d) Views of individual planes, with the bonds of the corresponding metallocycle colored in pink. Angles between yellow and green, green and turquois, turquois and yellow planes are 20.9°, 26.7°, 40.1°, respectively.

Voltammetric parameters of 1

Table S1. Redox potentials and cathodic-anodic peak separations of **1**. All potentials are referenced to the Fc$^+$/Fc couple.

Redox Couple	Ec (V)	Ea (V)	E1/2 (V)	ΔE (mV)
HITP$^{4-/5-}$	−1.50	−1.31	−1.41	0.19
HITP$^{4-/3-}$	−0.73	−0.65	−0.69	0.08
HITP$^{3-/2-}$	−0.14	−0.05	−0.10	0.09
HITP$^{2-/-}$	0.05	0.14	0.10	0.10

Variable-temperature EPR measurements of 1
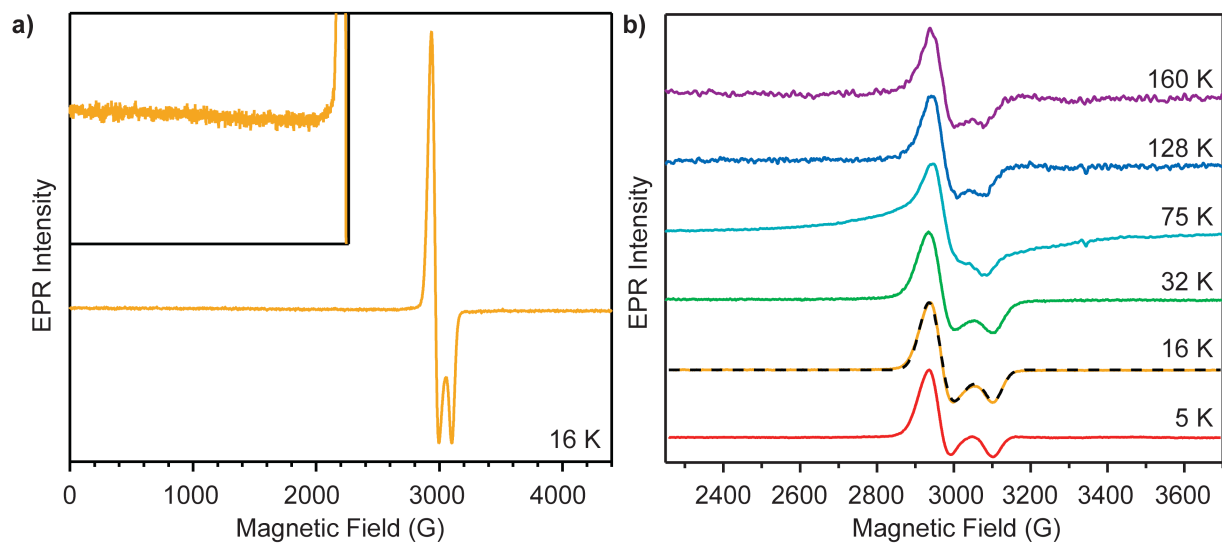
Figure S3. (a) EPR spectra of **1** as frozen solution in toluene glass measured at 16 K. Inset: zoom-in view of the 0-3000 G spectral region, showing the absence of signals with $g \geq 4$. (b) EPR spectra of **1** as frozen solution in toluene glass measured at 5 K (red), 16 K (orange), 32 K (green), 75 K (turquois), 128 K (blue), and 160 K (purple), respectively. The dashed black line corresponds to the fit described in text, with g_{eff} = 2.16, g_{Ni_1} = 2.21, J = −0.79 ± 0.01 cm^{-1}, $|D|$ = 30.23 ± 0.03 cm^{-1}.

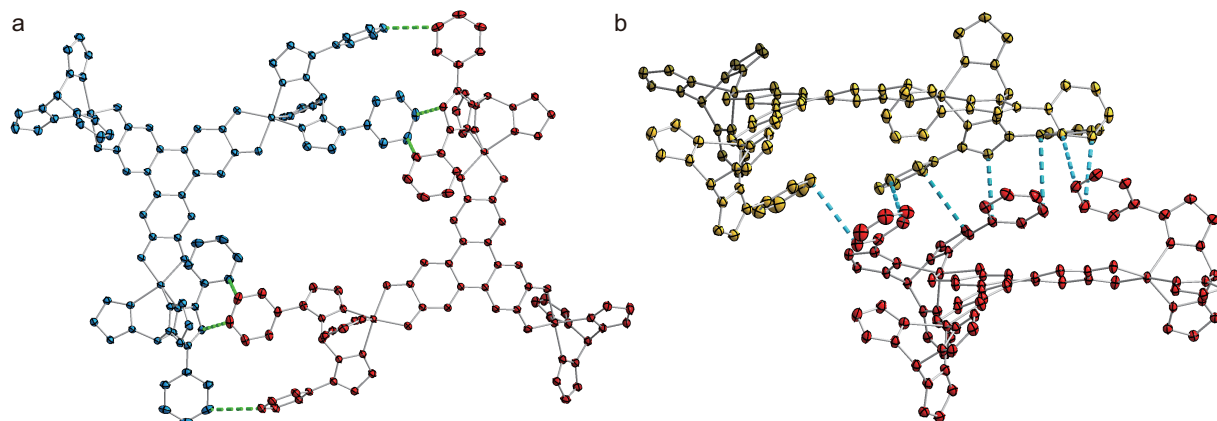**Magnetic susceptibility measurements of 1 under different magnetic fields**
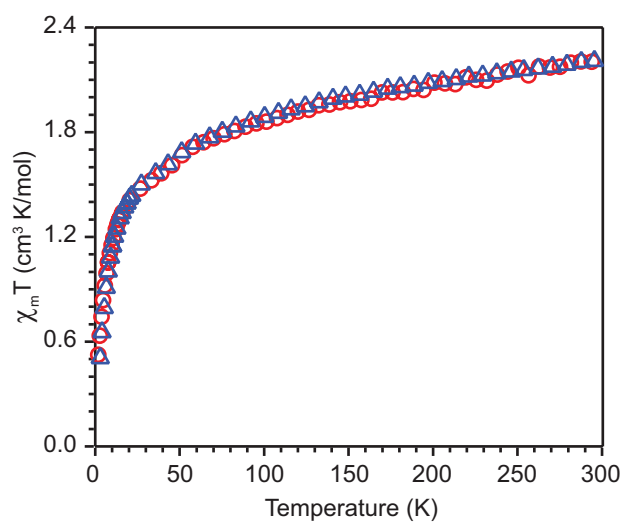
Figure S4. Temperature-dependent $\chi_m T$ curves for **1** under H = 1.0 kOe (red circles) and 10.0 kOe (blue triangles) in temperature range of 1.8 to 300 K.

Intermolecular interactions in crystal structure of 1

Figure S5. Crystal packing of **1** in (a) the same and (b) neighboring unit cells, with close contacts represented by green (a) and cyan (b) dashed lines. Individual molecules are colored in blue and red for (a), and yellow and red for (b). Phenyl groups on the Tp capping ligands are omitted for clarity if not involved in intermolecular interaction.

Fitting of the temperature dependence of $\chi_m T$ involves the term zJ describing intermolecular magnetic coupling according to Weiss molecular field theory, which adds the term $-zJ\langle S_z\rangle \boldsymbol{S}_z$ to $\mathcal{H}_1$ in the main text.[11] One possible source of intermolecular interactions in the aromatic stacking interaction, which takes place between closely-situated aromatic atoms.[12] Figure S5 plots selected C···C and C···N distances smaller than 3.8 Å between atom pairs on the phenyl and pyrazolyl rings. These aromatic stacking interactions commonly lead to intermolecular magnetic coupling of similar magnitude (0.1-2 cm^{-1}) in transition-metal complexes with capping groups containing aromatic moieties.[13,14]

Estimation of strong magnetic exchange in 1
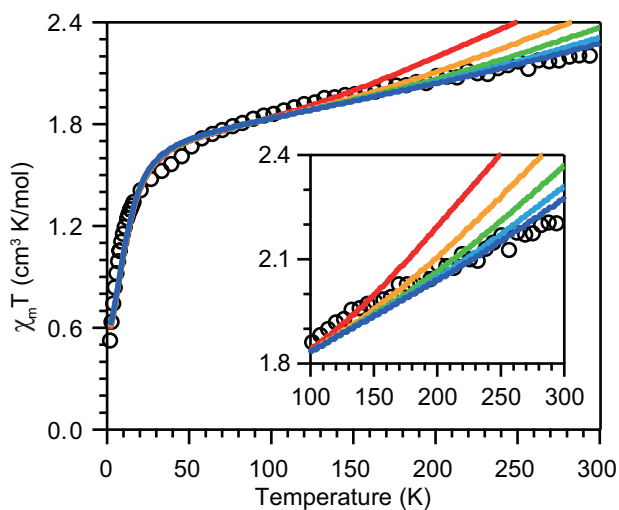
Figure S6. Simulations of the variable-temperature $\chi_m T$ of **1** using the Hamiltonian $\mathcal{H}_2$ in the main text, with $-J_1 = J_2 = 700$ cm^{-1} (red), 900 cm^{-1} (orange), 1100 cm^{-1} (green), 1300 cm^{-1} (cyan), and 1500 cm^{-1} (blue). Black empty circles are the experimental data. Inset is a zoom-in view of the high-temperature region.

Exchange coupling constants J_1 and J_2 are simulation using the Hamiltonian $\mathcal{H}_2$ described in the main text and parameters obtained from fitting to $\mathcal{H}_1$. g_{HITP} and g_{Ni23} are set to 2.0 and 2.16 based on the value of g_{eff} obtained from the $\mathcal{H}_1$ fit. Simulation revealed that while the low-temperature region is not affected by the magnitude of J_1 and J_2, satisfactory fit in the high-temperature region can only be obtained with $|J_1| = |J_2| \geq 1300$ cm^{-1}, providing a lower bound for the coupling constants.

Alternative spin models for 1

We note that the magnetic model presented here is derived from the best fit we could obtain to the magnetometry and EPR data. Based on the S = 1/2 spin state observed in EPR for HITP and three Ni, several possible combinations of spin states could be proposed as the starting point for the fitting process:

(1) $S(Ni^{2+})$ = +1, $S(Ni^{2+})$ = +1, $S(Ni^{2+})$ = -1, $S(HITP^{3-})$ = -1/2;

(2) $S(Ni^{2+})$ = 0, $S(Ni^{2+})$ = +1, $S(Ni^{2+})$ = -1, $S(HITP^{3-})$ = 1/2;

(3) $S(Ni^{2+})$ = 0, $S(Ni^{2+})$ = 0, $S(Ni^{2+})$ = +1, $S(HITP^{3-})$ = -1/2;

(4) $S(Ni^{3+})$ = -1/2, $S(Ni^{2+})$ = +1, $S(Ni^{2+})$ = -1, $S(HITP^{4-})$ = +1;

(5) $S(Ni^{3+})$ = +1/2, $S(Ni^{3+})$ = +1/2, $S(Ni^{2+})$ = -1, $S(HITP^{5-})$ = +1/2;

(6) $S(Ni^{3+})$ = +1/2, $S(Ni^{3+})$ = +1/2, $S(Ni^{3+})$ = -1/2, $S(HITP^{6-})$ = 0;

Here, 1 is the most appropriate spin model presented in the main text, and 2-6 are the alternative models tested by us. Although the presence of Ni^{3+} could already be ruled out based on crystallographic and electrochemical measurements, we still included combinations 4-6 to rule out unlikely situations. For 2, 4, 5, 6, no satisfactory fit could be obtained simultaneously for the susceptibility, magnetization and EPR data, with or without consideration of intermolecular interaction, temperature-independent paramagnetism, or zero-field splitting at the Ni centers. Whereas 3 gave satisfactory fits, as described in the main text, it is the phenomenological result from the strongly coupled Ni-HITP-Ni with effective S = 1/2, and ruled out by BS-DFT analysis. After obtaining the spin model described in the inset of Figure 3b in the main text, we tried to find this minimum from the starting point of 1. We were not able to find such minimum by floating all J(Ni-HITP) parameters, which always lead to unreasonable $|D|$ or χ_{TIP} values. Similar results were produced only by imposing large $|J_{1,2}|$ > 1000 cm^{-1}. Based on these concerns, and backed up by computational results, we believe model 1 is the most appropriate description for compound **1**.

Spin density distribution of the diamagnetic-Ni state of 1

a)

Ni^{2+}
S(Ni1) = 1

J *effective S = 1/2*

HITP^{3-}
S = 1/2

Ni^{2+} Ni^{2+}
S(Ni2) = 0   S(Ni3) = 0

b)
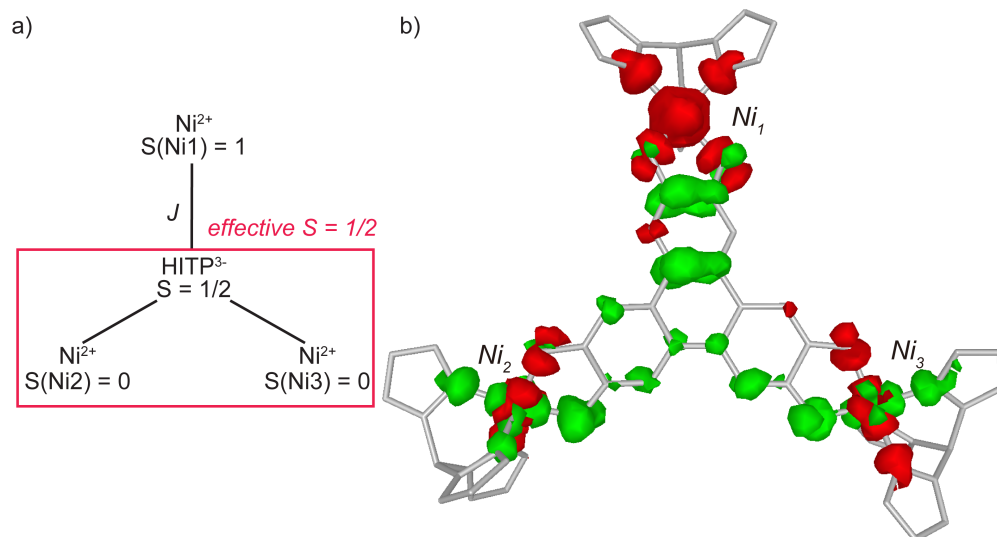
Figure S7. (a) Magnetic coupling scheme for the diamagnetic-Ni configuration of **1** as described in the main text. (b) Calculated spin density isosurfaces (0.0015 a.u.) in the diamagnetic-Ni state of **1**. Red and green represent positive and negative spin densities.

Calculated atomic spin distribution for the broken-symmetry state of 1

Table S2. Selected Löwdin charge and spin densities of the broken-symmetry state of **1**. HITP arm refers to the BQDI subunits making up the bridging ligand.

Atom	Löwdin charge density	Löwdin spin density
Ni_1	−0.85	1.14
Ni_2	−0.82	1.32
Ni_3	−0.81	−1.33
HITP Arm 1 (Ni_1)	0.33	−0.18
HITP Arm 2 (Ni_2)	0.33	−0.18
HITP Arm 3 (Ni_3)	0.35	0.09
Sum of three Ni	−2.48	1.13
Sum of HITP atoms	1.02	−0.27

Calculated atomic spin distribution for the diamagnetic-Ni state of 1

Table S3. Selected Löwdin charge and spin densities of the diamagnetic-Ni state of **1**. HITP arm refers to the BQDI subunits consisting the bridging ligand.

Atom	Löwdin charge density	Löwdin spin density
Ni_1	−0.86	1.24
Ni_2	−0.83	−0.08
Ni_3	−0.83	0.01
HITP Arm 1 (Ni_1)	0.31	−0.10
HITP Arm 2 (Ni_2)	0.35	−0.12
HITP Arm 3 (Ni_3)	0.34	−0.09
Sum of three Ni	−2.52	1.13
Sum of HITP atoms	0.99	−0.27

Crystallographic table for 1

Table S4. Crystal data and structure refinement for **1**

Deposition number	2109142
Empirical formula	$C_{165}H_{141}B_3N_{15}Ni_3$, $2CH_2Cl_2$
Formula weight	2838.42
Temperature	100(2)
Wavelength	0.71073 Å
Crystal system	Triclinic
Space group	$P\bar{1}$
Unit cell dimensions	a = 13.9935(6) Å
	b = 18.2318(8) Å
	c = 30.6238(13) Å
	α = 103.088(2) °
	β = 99.793(2) °
	γ = 91.711(2) °
Volume	7480.1(6) Å^3
Z	2
Density (calculated)	1.260 mg/m^3
Absorption coefficient	0.506 mm^{-1}
F (000)	2964
Crystal size	0.22 x 0.19 x 0.01 mm^3
θ range for data collection	1.388 to 31.068°
Index ranges	$-20 \leq h \leq 20$, $-26 \leq k \leq 26$, $-44 \leq l \leq 44$
Reflections collected	47922
Independent reflections	14169
Completeness to θ_{max}	99.9%
Absorption correction	Multi-scan
Max. and min. transmission	0.7462 and 0.6943
Refinement method	Full-matrix least-squares on F^2
Data / restraints / parameters	47922 / 2976 / 1851
Goodness-of-fit[a] on *F^2*	1.034
R$_1$[b]	0.0491
wR$_2$[c]	0.1226

[a] GOF = $\left(\frac{\Sigma w(F_o^2 - F_c^2)^2}{n-p}\right)^{\frac{1}{2}}$ where *n* is the number of data and *p* is the number of parameters refined.

[b] $R_1 = \frac{\Sigma ||F_o| - |F_c||}{\Sigma |F_o|}$. [c] $wR_2 = \left(\frac{\Sigma (w(F_o^2 - F_c^2)^2)}{\Sigma (w(F_o^2)^2)}\right)^{\frac{1}{2}}$.

Selected bond lengths and angles of 1
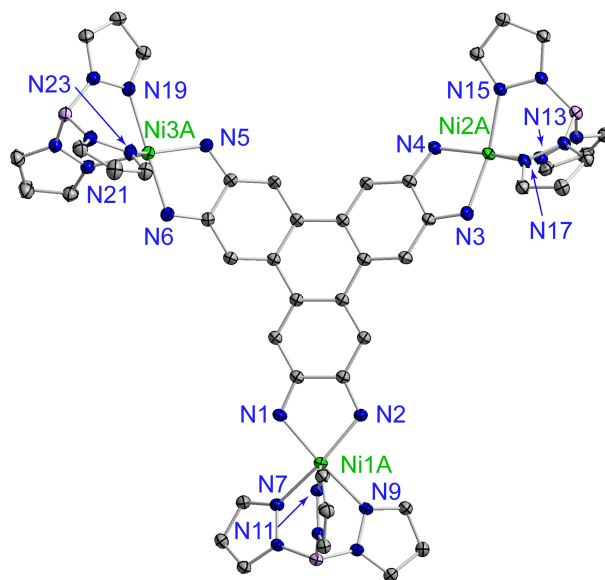
Figure S8. Labels of selected atoms in **1**. Atoms share the same labeling scheme as in the crystallographic data file.

Table S5. Selected bond lengths of **1**. Atomic labeling scheme follows Figure S8.

Atom1	Atom2	Length (Å)
Ni1A	N1	1.985(2)
Ni1A	N2	1.969(2)
Ni1A	N7	2.071(2)
Ni1A	N9	2.112(2)
Ni1A	N11	2.018(1)
Ni2A	N3	2.007(2)
Ni2A	N4	1.967(2)
Ni2A	N13	2.022(1)
Ni2A	N15	2.088(1)
Ni2A	N17	2.066(2)
Ni3A	N5	1.939(2)
Ni3A	N6	2.021(2)
Ni3A	N19	2.128(2)
Ni3A	N23	2.021(1)
Ni3A	N21	2.042(2)

Table S6. Selected bond angles of **1**. Atomic labeling scheme follows Figure S8.

Atom1	Atom2	Atom3	Angle (°)
N1	Ni1A	N2	80.16(7)
N1	Ni1A	N7	92.39(6)
N1	Ni1A	N9	161.47(6)
N1	Ni1A	N11	109.23(6)
N2	Ni1A	N7	159.48(7)
N2	Ni1A	N9	96.25(6)
N2	Ni1A	N11	108.13(6)
N7	Ni1A	N9	84.74(6)
N7	Ni1A	N11	92.36(6)
N9	Ni1A	N11	89.20(6)
N3	Ni2A	N4	80.13(6)
N3	Ni2A	N13	105.00(6)
N3	Ni2A	N15	165.34(6)
N3	Ni2A	N17	91.47(6)
N4	Ni2A	N13	114.76(6)
N4	Ni2A	N15	96.46(6)
N4	Ni2A	N17	152.76(6)
N13	Ni2A	N15	89.41(6)
N13	Ni2A	N17	92.41(6)
N15	Ni2A	N17	85.13(6)
N5	Ni3A	N6	80.46(7)
N5	Ni3A	N19	97.53(7)
N5	Ni3A	N23	122.94(7)
N5	Ni3A	N21	144.81(7)
N6	Ni3A	N19	176.41(7)
N6	Ni3A	N23	94.80(7)
N6	Ni3A	N21	94.95(7)
N19	Ni3A	N23	88.79(6)
N19	Ni3A	N21	84.98(6)
N23	Ni3A	N21	92.12(6)

Geometric distortion of the Ni atoms in 1

Table S7. Continuous-shape measurements of **1**. Atomic labeling scheme follows Figure S8.

Atom	S_{TBP}	S_{SP}
Ni1A	6.12	1.02
Ni2A	4.46	1.21
Ni3A	2.65	2.85

Continuous shape measure (S), first proposed by Cirera et al., offers a description for the degree of distortion of the coordination sphere of a metal atom from an ideal polyhedron.[15] According to reference 14, S is defined by the following equation:

$$S = \min \frac{\sum_{k=1}^{N} |\overrightarrow{Q_k} - \overrightarrow{P_k}|^2}{\sum_{k=1}^{N} |\overrightarrow{Q_k} - \overrightarrow{Q_0}|^2} \times 100$$

where $\overrightarrow{Q_k}$ and $\overrightarrow{Q_0}$ correspond to the position vectors of the N atoms and the geometrical center of the coordination sphere of the metal atom under investigation, and $\overrightarrow{P_k}$ represents the position vectors of the ideal polyhedron closest in size and orientation. While S ranges from 0 to 100, S = 0 corresponds to the case when the coordination sphere of the metal atom is in perfect agreement with the ideal polyhedron. For **1**, the Ni coordination spheres are analyzed by comparing with ideal trigonal bipyramid (S_{TBP}) and square planar (S_{SP}) geometries. As can be seen in Table S7, the coordination spheres of Ni1A and Ni2A are best described as square planar. On the other hand, the coordination sphere of Ni3A can be described as both trigonal bipyramid and square planar, with the former being a slightly better description.

References

1   L. Chen, J. Kim, T. Ishizuka, Y. Honsho, A. Saeki, S. Seki, H. Ihee and D. Jiang, *J. Am. Chem. Soc.*, 2009, **131**, 7287–7292.

2   Y. Wang, F. Lambert, E. Rivière, R. Guillot, C. Herrero, A. Tissot, Z. Halime and T. Mallah, *Chem. Commun.*, 2019, **55**, 12336–12339.

3   G. M. Sheldrick, *Acta Crystallogr. Sect. C Struct. Chem.*, 2015, **71**, 3–8.

4   S. Alvarez, P. Alemany, D. Casanova, J. Cirera, M. Llunell and D. Avnir, *Coord. Chem. Rev.*, 2005, **249**, 1693–1708.

5   N. F. Chilton, R. P. Anderson, L. D. Turner, A. Soncini and K. S. Murray, *J. Comput. Chem.*, 2013, **34**, 1164–1175.

6   S. Stoll and A. Schweiger, *J. Magn. Reson.*, 2006, **178**, 42–55.

7   F. Neese, *WIREs Comput. Mol. Sci.*, 2012, **2**, 73–78.

8   F. Neese, *WIREs Comput. Mol. Sci.*, , DOI:10.1002/wcms.1327.

9   A. D. Becke, *Phys. Rev. A*, 1988, **38**, 3098–3100.

10   F. Weigend, *Phys. Chem. Chem. Phys.*, 2006, **8**, 1057–1065.

11   O. Kahn, *Molecular Magnetism*, VCH Publishers, Inc., 1993.

12   C. R. Martinez and B. L. Iverson, *Chem. Sci.*, 2012, **3**, 2191–2201.

13   M. Bubnov, A. Cherkasova, I. Teplova, E. Kopylova, G. Fukin, M. Samsonov, A. Bogomyakov, S. Fokin, G. Romanenko, V. Cherkasov and V. Ovcharenko, *Polyhedron*, 2016, **119**, 317–324.

14   C. G. Pierpont and A. S. Attia, *Collect. Czechoslov. Chem. Commun.*, 2001, **66**, 33–51.

15   J. Cirera, E. Ruiz and S. Alvarez, *Organometallics*, 2005, **24**, 1556–1562.